scientific reports

OPEN

Revealing exchange bias in spin compensated systems for spintronics applications

Koustav Pal[1✉], Suman Dey[1], Aftab Alam[2] & I. Das[1]

Antiferromagnetic materials offer potential for spintronic applications due to their resilience to magnetic field perturbations and lack of stray fields. Achieving exchange bias in these materials is crucial for certain applications; however, discovering such materials remains challenging due to their compensated spin structure. The quest for antiferromagnetic materials with exchange bias became a reality through our experimental study and theoretical simulation on Sr_2FeIrO_6 and Sr_2CoIrO_6. This study also unveils the impact of ionic disorder and lattice distortion on magnetic properties. The presence of exchange bias in both materials, given their antiferromagnetic nature, is intriguing. This study opens up new avenues for achieving exchange bias in spin-compensated systems, offering potential for low power and ultra fast antiferromagnetic spintronic applications in future research endeavors.

Keywords Perovskite, Antiferromagnetic Exchange bias, Spin glass, Disorder

Antiferromagnetic materials show promise for future spintronic applications due to their unique attributes, including robustness against magnetic field perturbations, absence of stray fields, rapid dynamics, and capability to induce significant magnetotransport effects. Exchange bias (EB) further enhances their utility[1–4]. However, the conventional method of introducing a ferromagnetic (FM) layer in multilayer thin films to induce EB presents a drawback by adding an extra layer and increasing vulnerability to external magnetic fields[5–9]. Ideally, an antiferromagnet with EB independent of composition inhomogeneity or frustrated spins (spin glass) would be preferable. Numerous experimental and theoretical studies have illuminated the fact that the EB effect can be intentionally engineered in a plethora of heterostructures. Examples include inhomogeneous magnetic phases like FM/ferrimagnetic (FiM), FM/spin glass (SG), FM/ antiferromagnetic (AFM), hard/soft FM systems, magnetic nanoparticles, granular composites, bilayers, and superlattices[10–18]. The comprehension of these systems cannot elucidate the origin of EB in spin-compensated AFM systems which makes achieving EB in spin-compensated systems more challenging.

In a recent study involving a thin film system comprising two distinct types of AFM materials (chiral-antiferromagnet Mn_3Sn and collinear-antiferromagnet MnN), EB was observed due to the interfacial energy between the two different AFM materials[19]. However, generating EB in a single-phase AFM bulk compound presents a greater challenge. Regarding spin-compensated AFM systems, perovskite compounds play a significant role due to their remarkable ability to accommodate various ions from a wide range of the periodic table, resulting in tunable electronic and magnetic properties. With in perovskite compounds in recent times, iridium (Ir) based double perovskites, denoted as A_2BIrO_6 (with a specific emphasis on B belonging to the 3d element category), have attracted substantial attention in the condensed matter physics community. The interest of these materials arises from the fact that 3d transition metals manifest significant electronic correlation, a characteristic noticeably diminished in 5d elements. Concurrently, there is a notable increase in the strength of the spin-orbit coupling effect as the d character rises from 3d to 5d elements. There are few study on this group of 3d-5d interacting system Sr_2BIrO_6 (B = Fe, Co, Ni, Cu, Zn) which are AFM[20–23].

In these compounds the electronic structure, as well as magnetic and transport properties, can be tuned by altering the local environment and symmetry. Through a small rearrangement of these interaction energies, intriguing physical properties such as topologically insulating behavior, superconductivity, Weyl semimetallic states, quantum spin liquid phases, etc., are predicted in these materials[24–29]. While EB is typically not expected in spin-compensated systems, few theoretical studies have proposed that EB can occur in these systems via the Dzyaloshinsky-Moriya (DM) interaction[30–32].

[1]Saha Institute of Nuclear Physics, A CI of Homi Bhabha National Institute, Kolkata 700064, India. [2]Department of Physics, Indian Institute of Technology Bombay, Mumbai 400076, India. ✉email: koustav.pal97@gmail.com

The manifestation of EB via the DM interaction in bulk AFM materials has not been previously observed. Consequently, the search for new materials exhibiting EB through this mechanism is of significant interest and highly demanding. Beyond DM interaction, the profound impact of ionic disorder and structural distortion on this phenomenon is also notable. We have brought out the existence of EB in two spin-compensated Ir based compounds, Sr_2FeIrO_6 and Sr_2CoIrO_6, and examined the impact of ionic disorder and lattice distortion on their magnetic properties through experimental findings and theoretical simulations.

Experimental details

Polycrystalline Sr_2FeIrO_6 (SFI) and Sr_2CoIrO_6 (SCI) samples were synthesized using the solid-state reaction method. The synthesis involved meticulously mixing $SrCO_3$, Fe_2O_3, and IrO_2 powders, as well as $SrCO_3$, Co_3O_4, and IrO_2 powders, each with a purity of 99.995%, in stoichiometric proportions, followed by grinding. The mixture underwent heating at 950 °C for 16 hours, followed by regrinding and heating at 1050 °C for 24 hours. Afterward, it was regrinded, pelletized, and finally subjected to heating at 1150 °C for 72 hours. The resulting fine powder samples were analyzed using X-ray diffraction (XRD) measurements performed with a Rigaku X-Ray diffractometer, utilizing Cu-Kα radiation. The XRD scans covered an angular range (2θ) of 20–90°. Rietveld refinement technique was employed using the FULLPROF SUITE software[33,34]. The structural figures of the compounds were generated using VESTA software[35].

The polycrystalline sample underwent extensive grinding and sonication to produce small, thin samples suitable for Transmission Electron Microscopy (TEM) imaging. Subsequently, these samples were deposited onto copper grids for TEM imaging, High-Resolution Transmission Electron Microscopy (HRTEM) imaging, Energy Dispersive X-ray Spectroscopy (EDX) analysis and elemental mapping. TEM measurements of SFI and SCI was conducted using an FEI Tecnai G^2 F30-ST instrument operating at 300 kV. This instrument was equipped with a high-angle annular dark-field (HAADF) detector from Fischione (model 3000) for Bragg scattering-free imaging and an energy-dispersive X-ray (EDX) spectroscopy attachment for compositional analysis. X-ray photoelectron spectroscopy (XPS) measurements were conducted using an Omicron Nanotechnology ultrahigh vacuum (UHV) multiprobe setup. The setup included an EA125 hemispherical energy analyzer and an Al Kα X-ray source. The XPS data was fitted using a Shirley background and a Gaussian Lorentzian curve. The grain size of the synthesized sample was determined by analyzing scanning electron microscopy (SEM) images captured with the Zeiss Supra 40 instrument. Moreover, various magnetic measurements, including isothermal magnetization ($M(H)$), temperature-dependent magnetization ($M(T)$), and magnetic relaxation ($M(t)$), were conducted using a commercial SQUID magnetometer from Quantum Design.

Results and discussions
Structural characterization

In Fig. 1a and b, the XRD patterns of SFI and SCI are presented, accompanied by their respective full Rietveld refinement fittings. Notably, the crystal structure of the compounds crystallizes in different space groups depending on the synthesis methods and the size of the A-site atom[36–39]. During our analysis, we explored
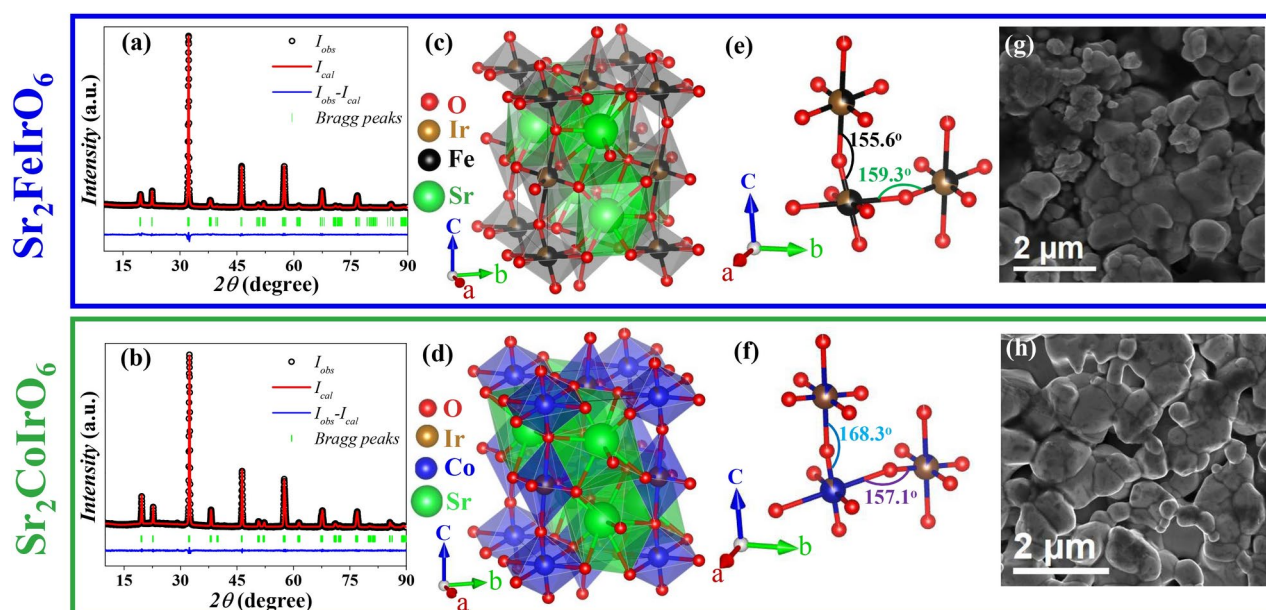

Fig. 1. (**a**) Full Reitveld refinement of the XRD spectrum of powdered polycrystalline (**a**) Sr_2FeIrO_6 and (**b**) Sr_2CoIrO_6 compound recorded at 300 K; Triclinic crystal structure of the double perovskite (**c**) Sr_2FeIrO_6 and (**d**) Sr_2CoIrO_6 compound. The Fe(/Co)O_6 and IrO_6 octahedra are shown with Fe(/Co) (black(/blue)) and Ir (brown) at the center surrounded by the oxygen (red). Atom at the center of the cube is Sr (green); Local environment of (**e**)FeO_6, IrO_6 and (**f**) CoO_6, IrO_6; SEM Imaging of (**g**) Sr_2FeIrO_6 and (**h**) Sr_2CoIrO_6.

various possible space groups, with the best fit observed for a triclinic crystal symmetry in the I-1 space group (space group number 2)[40]. However, there remains a small peak near 28.9° that is not well-fitted with this space group, which we attribute to the influence of the silica substrate holder[41]. The lattice parameters of the structure SFI is determined to be: a = 5.55(7) Å, b = 5.55(3) Å, c = 7.86(3) Å, α = 89.57(1)°, β = 90.74(3)° and γ = 89.67(1)°. For SCI the lattice parameters are a = 5.54(4) Å, b = 5.55(2) Å, c = 7.84(1) Å , α = 90.02(0)°, β = 89.67(1)° and γ = 90.15(5)°. The refined lattice parameters, atomic coordinates and reliability factors for SFI and SCI have been presented in the supplementary Sect. I. The crystal structure includes two Wyckoff positions for Fe (Co) and Ir, specifically 2a and 2e. Thus, we performed the Full Rietveld Refinement analysis using the order parameter as a free parameter. In the SFI compound, we found a 60% ordering between Fe and Ir, whereas in the SCI compound, there is a 90% ordering between Co and Ir.

We have presented the Full Rietveld Refinement fittings at 60% and 90% order for both compounds in Supplementary Sect. I to better comprehension. Figure. 1c and d visually represent the perovskite unit cell for SFI and SCI. In the triclinic structure of SFI (SCI), the 2a(0,0,0) and 2e(0,0,0.5) sites show 60% (90%) ordering of Fe (Co) and Ir. Fe (Co) and Ir are represented by the colors black (blue) and brown, respectively, while a central Sr ion is depicted in green. From the lattice parameters, it is clear that the α, β and γ for SCI is more close to 90° than SFI , which indicated SFI structure is more distorted than SCI. In Fig. 1e and f, the local environment of the Fe(Ir)O$_6$ and Co(Ir)O$_6$ octahedra is displayed. These octahedra exhibit distortion and disorder. In SFI structure in plane Fe/Ir–O–Fe/Ir bond angle measures 159.3° and out of plane bond angle measures 155.6°. In SCI structure in plane Co/Ir–O–Co/Ir bond angle measures 157.1° and out of plane bond angle measures 168.3°. This also indicates the higher out of plane distortion in SFI than SCI. The structural analysis clearly indicates that SFI exhibits more structural distortion and ionic disorder in the 2a–2e sites.

SEM was employed to evaluate the grain size of the synthesized sample. Figure 1g and h depict SEM images of the synthesized SFI and SCI samples respectively. The analysis reveals an average particle size in the micron range, emphasizing the bulk nature of the system.

To comprehend the crystallinity of the particles and the impact of disorder, we conducted TEM and HRTEM imaging. Figure 2 a and b depict the TEM images of the SFI and SCI compounds, respectively. The particles exhibit well-defined crystallinity up to the grain boundary, with no observable amorphous regions. HRTEM images of the SFI and SCI compounds are presented in Fig. 2c and d, respectively, revealing atomic resolution and crystalline structure. To further elucidate the details, we performed inverse fast Fourier transform (IFFT) analysis on the area marked by the red box in the HRTEM images, as shown in Fig. 2e and f. While atomic resolution is achieved for the SFI compound (Fig. 2e), the presence of substantial disorder (60% Fe and Ir) results in intensity averaging, making it challenging to distinguish individual atoms. Conversely, in Fig. 2f, distinct intensity variations are observed due to the ordered Co and Ir structure, as highlighted by the yellow circle. Based on TEM imaging, it can be inferred that SCI possesses a more ordered structure compared to SFI. We conducted elemental mapping to analyze the constituent elements of the SFI and SCI compounds. Figure 3a and h display the STEM-HAADF images of the particles on which elemental mapping was conducted for SFI and
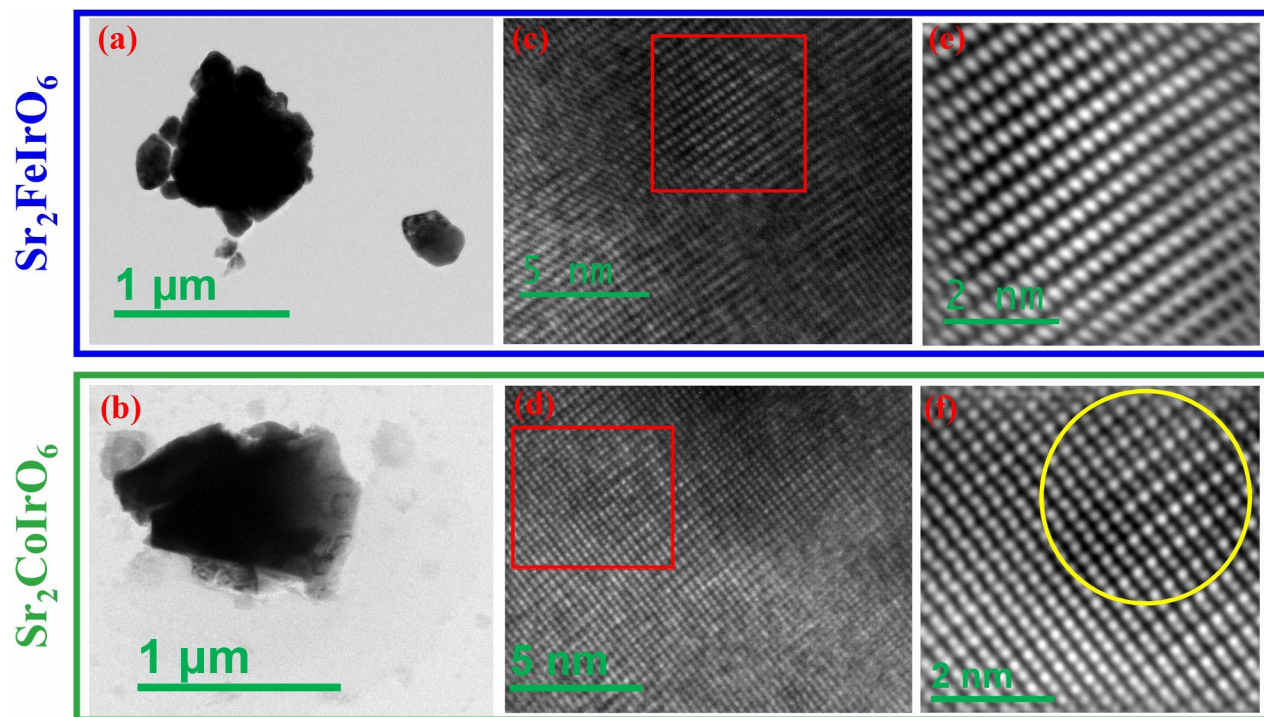

Fig. 2. TEM image for (**a**) Sr$_2$FeIrO$_6$ (**b**) Sr$_2$CoIrO$_6$; HRTEM image for (**c**) Sr$_2$FeIrO$_6$ (**d**) Sr$_2$CoIrO$_6$; IFFT of the red box area of the HRTEM image for (**e**) Sr$_2$FeIrO$_6$ (**f**) Sr$_2$CoIrO$_6$.
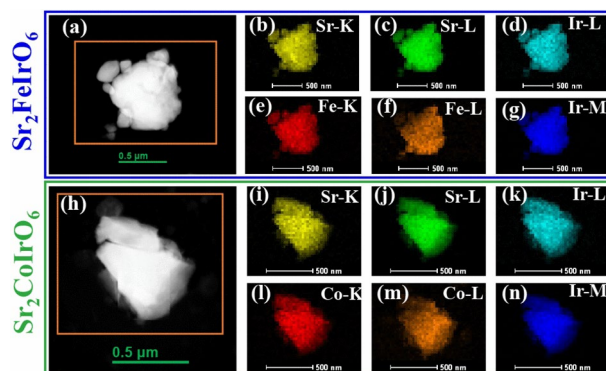
Fig. 3. STEM-HAADF image of the particle on which Elemental mapping was performed for (**a**) Sr_2FeIrO_6, (**h**) Sr_2CoIrO_6; Elemental mapping of the constituent element for (**a**)–(**g**) Sr, Fe,Ir for Sr_2FeIrO_6 and (**i**)–(**n**) Sr,Co,Ir for Sr_2CoIrO_6.
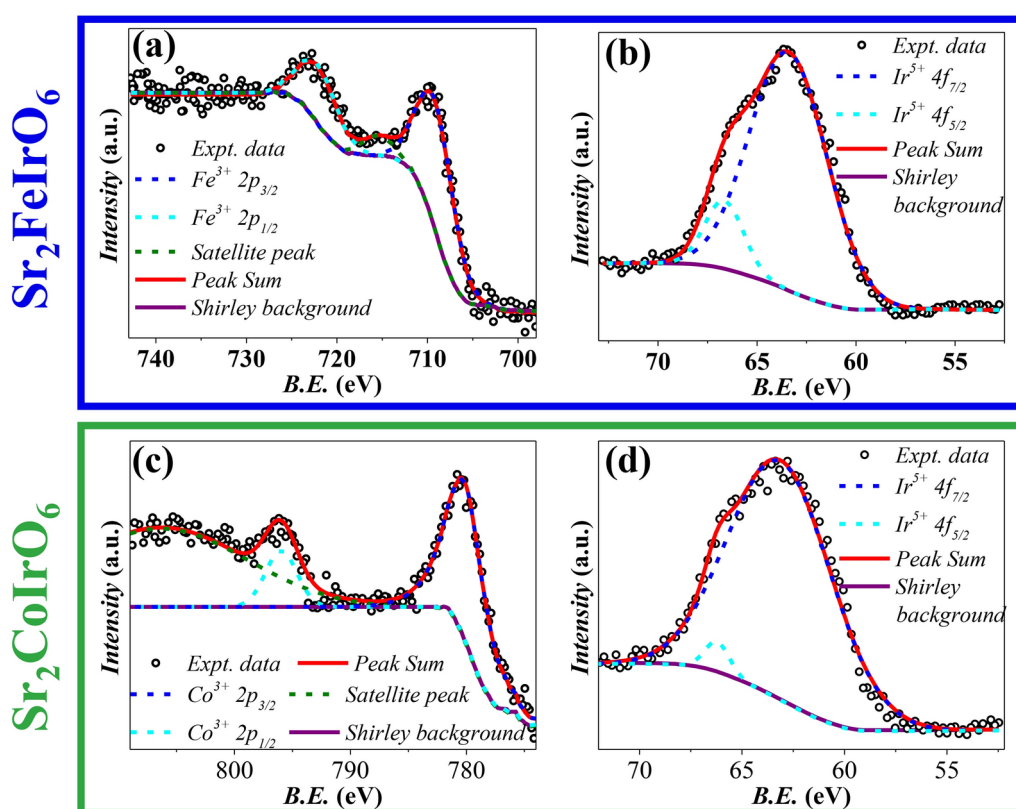
Fig. 4. XPS spectra of core levels: (**a**) Fe 2p; (**b**) Ir 4f for Sr_2FeIrO_6; and (**c**) Co 2p and (**d**) Ir 4f for Sr_2CoIrO_6.

SCI, respectively. Figure 3b–g illustrate the elemental mapping of the constituent elements (Sr, Fe, and Ir) for SFI, while Fig. 3i–n depict the elemental mapping for SCI (Sr, Co, and Ir). In both instances, we observed no inhomogeneity in the images within our resolution limit. We also conducted EDAX analysis of the compound, confirming that the atomic percentage matched our chemical composition (shown in the supplementary Sect. I).

In our exploration of the oxidation states of the metal ions within the compound, we carefully analyzed core-level XPS spectra for Fe 2p, Co 2p, and Ir 4f. Figure 4 present the analysis of Co, Fe, and Ir core-level XPS spectra for both the SFI and SCI compounds. The sample underwent X-ray irradiation, and the core-level spectra were obtained by simultaneously measuring emitted electron counts and their associated kinetic energies. These figures showcase the spin-orbit split components alongside the deconvoluted peaks.

To evaluate the ionic composition, we analyzed core-level XPS spectra for Fe 2p, Co 2p, and Ir 4f. Figure 4a and b depict the analysis of Fe and Ir core-level XPS spectra for the SFI compound. In Fig. 4a, peaks at 709.07 eV

and 722.06 eV correspond to the $2p_{3/2}$ and $2p_{1/2}$ states of Fe, indicating Fe^{3+} ions[42–44]. In Fig. 4b, peaks at 63.4 eV and 66.65 eV correspond to the $4f_{7/2}$ and $4f_{5/2}$ states of Ir, signifying Ir^{5+} ions[45,46].

Figures 4c and d illustrate the XPS analysis of Co and Ir for the SCI compound. In Fig. 4c, peaks at 780.10 eV and 795.97 eV correspond to the $2p_{3/2}$ and $2p_{1/2}$ states of Co, representing Co^{3+} ions, with a satellite peak at 806.32 eV[47,48]. In Fig. 4d, peaks at 63.1 eV and 66.2 eV signify the $4f_{7/2}$ and $4f_{5/2}$ states of Ir, indicating the presence of Ir^{5+} ions[45,46].

Magnetic properties

To comprehend the magnetic interactions within the system, a series of magnetic measurements were conducted. The magnetization was recorded as a function of temperature ($M(T)$), employing both the zero-field cooled (ZFC) and field-cooled (FC) protocols across a temperature range of 3-380 K at various magnetic fields. Figure 5a and b illustrate the $M(T)$ plots under magnetic fields of 500 Oe, 1 Tesla, and 7 Tesla for SFI and SCI compounds. To consolidate the three $M(T)$ plots into a single graph, we scaled the magnetization by a factor specified in the figure, located just below each plot ($M^* = M \times factor$). For SFI, the transition temperature (T_N) is 60 K, but for SCI, it is significantly higher at about 130 K. Although AFM interactions constitute the predominant interaction in both compounds, the somewhat smaller T_N in the SFI compound raises the possibility of magnetic frustration due to its greater degree of structural disorder in the magnetic ion arrangement relative to the SCI compound. At high magnetic fields, the FC curve in the SCI compound drops around 130 K, corresponding to the AFM transition temperature. Notably, the FC $M(T)$ curve for the SFI compound shows a trend towards saturation followed by an increase, which can be attributed to the alignment of frustrated spins along the external magnetic field direction due to the reduction in thermal energy at lower temperatures[49,50]. This behavior is characteristic of spin glass materials. In contrast, the FC $M(T)$ curve for the SCI compound decreases after the transition temperature, driven by the alignment and anti-alignment of spins due to AFM ordering[23,51]. These results distinctly underscore the different magnetic behaviors of the two compounds. At temperatures below 15 K, both compounds display an upturn, attributable to the low crystallographic symmetry coupled with the spin-orbit coupling (SOC) present in Sr_2BIrO_6 (B = Fe, Co) compounds. This combination facilitates a distinctive antisymmetric DM interaction, leading to the emergence of weak ferromagnetism (WFM)[52,53]. This WFM component arising from a slight canting of the antiferromagnetically ordered moments of the Fe(Co) and Ir sub-lattices at low temperatures. This behavior is reminiscent of the situation observed in Ir-based double perovskites[54]. The increase in a higher applied DC magnetic field diminishes the distinction between the FC and ZFC states at low temperature.

To enhance our comprehension of the magnetic interaction, we study the inverse susceptibility data for both compounds within the paramagnetic (PM) region and performed a fitting using the Curie-Weiss law (CW).
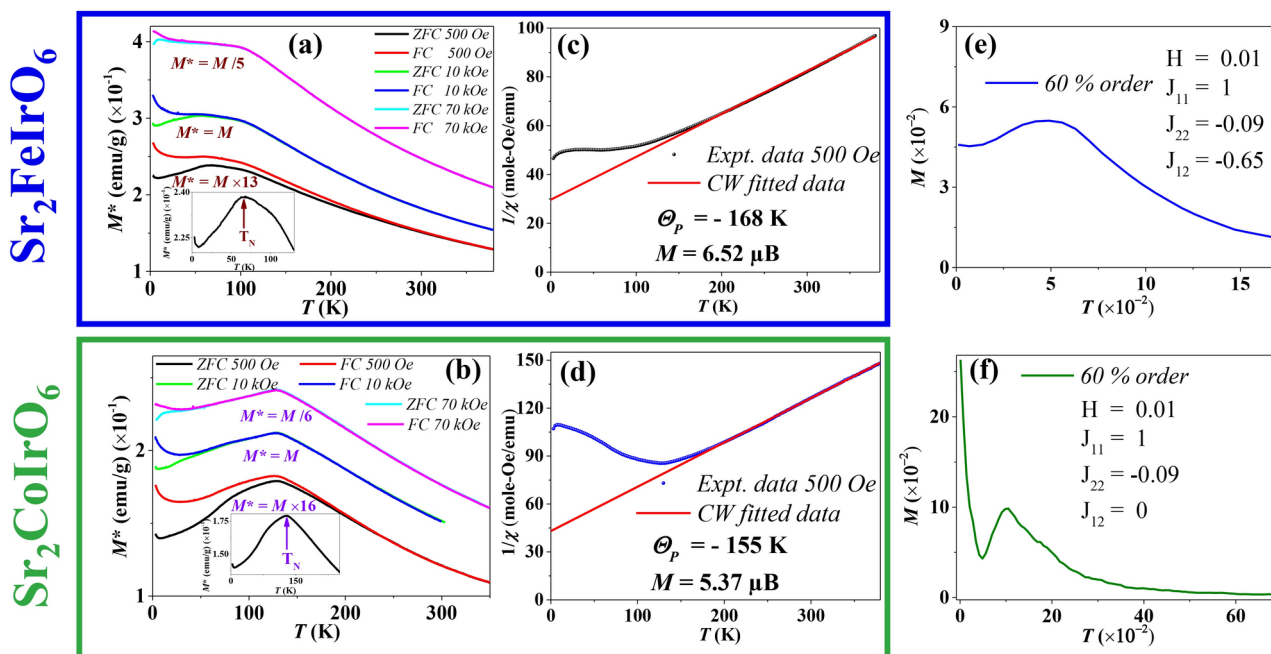

Fig. 5. ZFC and FC $M(t)$ of (**a**) Sr_2FeIrO_6 and (**b**) Sr_2CoIrO_6, To incorporate three $M(T)$ plots into a single graph, we have scaled the magnetization by a factor indicated in the figure, provided just below each plot; Inverse susceptibility as a function of temperature for $H = 500$ Oe of (**c**) Sr_2FeIrO_6 and (**d**) Sr_2CoIrO_6 compound; Theoretically simulated ZFC $M(T)$ curves with 60% disorder, where (**e**) depicts $J_{12} = -0.65$ and (**f**) depicts $J_{12} = 0$.

$$\chi = \frac{C}{T - \Theta_P} \tag{1}$$

where Θ_P denotes the paramagnetic Curie temperature and C stands for the Curie constant. Our fitting procedure covered the paramagnetic range, extending from 175 K (190 K) to 380 K for SFI (SCI). The solid red line in Fig. 5c and d represents the closely aligned fitted data (red line) in comparison to the experimental data points (depicted by black and blue symbols for the SFI and SCI compounds). The effective PM moment (μ_{eff}^{exp}) is calculated using the formula $\mu_{eff}^{exp} = \sqrt{3k_B C / N_A}$, where k_B denotes the Boltzmann constant, and N_A represents the Avogadro number[15].

Based on the earlier theoretical calculations and the combined findings from the Density of States and calculated magnetic moments, we can use the result that Fe is in the +3 ($3d^5$) electronic state with a high spin state of S = 5/2, while Ir is in the +5 ($5d^4$) electronic state with a low intermediate state of S = 1[55]. Using this we can calculate the theoretical μ_{eff}^{theory} using the formula $\mu_{eff}^{theory} = \sqrt{(\mu_{Fe})^2 + (\mu_{Ir})^2}$, where μ_{Fe} and μ_{Ir} represent the magnetic moments of Fe^{3+} and Ir^{5+} cations, respectively. Applying the provided equation along with the ionic state of Fe and Ir, μ_{eff}^{theory} is computed to be 6.56 μ_B, aligning closely with the experimental value of 6.52 μ_B. There are also reports suggesting that Ir^{5+} may exist in the $S = 0$ spin state[23,56–60]. However, based on this spin state, the theoretical effective magnetic moment, μ_{eff}^{theory}, is calculated to be 5.9 μ_B, which is significantly smaller than our experimental value. Consequently, we do not consider the $S = 0$ state for Ir^{5+} in our analysis, but instead adopt the $S = 1$ state for calculations[40,55].

For SCI, we can calculate the theoretical effective magnetic moment, $\mu_{eff}^{theory} = \sqrt{(\mu_{Co})^2 + (\mu_{Ir})^2}$, where μ_{Co} and μ_{Ir} represent the magnetic moments of Co^{3+} and Ir^{5+} cations, respectively. Co is in the +3 ($3d^6$) electronic state with a **high spin state** of S = 2, while Ir is in the +5 ($5d^4$) electronic state with S = 1[23,61]. Utilizing this data alongside the ionic states of Co and Ir, the theoretical effective magnetic moment (μ_{eff}^{theory}) is calculated to be 5.65 μ_B, closely matching the experimental value of 5.37 μ_B.

From the CW fit, we calculated θ_P, for the SFI and SCI compounds as $-$ 168 K and $-$ 155 K, respectively. These negative values suggest that the dominating interaction is AFM. Calculating the ratio $\frac{|\theta_P|}{T_N}$ for the SFI and SCI compounds yields 2.8 and 1.2, respectively. This further indicates SFI compound is far more frustrated than SCI.

To investigate the relationship between T_N and disorder, as well as the cause of the low temperature increment in $M(T)$, Monte Carlo simulations were performed. Detailed methods and the consideration of various interactions are provided in the supplementary Sect. II. To explore the effect of disorder, simulations were conducted at different percentages of magnetic ions ordering. Figure 5e presents the zero-field-cooled (ZFC) plot for $J_{11} = 1.0$, $J_{22} = -0.09$, and $J_{12} = -0.65$ at $H = 0.01$, where J_{11} and J_{22} represent the nearest-neighbor interactions of Fe-Fe and Ir-Ir, respectively, and J_{12} denotes the nearest-neighbor interaction between Fe and Ir[55]. This plot exhibits reasonable agreement with ZFC experimental data. Analyzing order percentages ranging from 100 to 60% reveals a shift of T_N to lower temperatures and a decrease in the peak magnetization value with decreasing order (supplementary Sect. III). This observation supports the claim that higher disorder in SFI corresponds to a lower T_N. Additionally, adjusting interaction parameters elucidates their impact on $M(T)$; specifically, setting $J_{12} = 0$ amplifies the upturn at low temperatures, as depicted in Fig. 5f in contrast to our experimental observation.

To comprehend the ground state of the systems, we conducted ZFC $M(H)$ measurements at different temperatures, as illustrated in Fig. 6a and b for the SFI and SCI compounds. The ZFC $M(H)$ loops exhibit a symmetric nature and there is a small hysteresis in the curves, below the T_N temperature, may indicate the presence of some WFM arising from DM interaction in AFM[62]. It is noteworthy that even under a 7-tesla magnetic field, the magnetization does not reach saturation, nor does it show any tendency to saturate. Instead, it increases linearly, indicating the presence of a strong AFM interaction.

To delve deeper into the magnetic behavior of the compounds, we conducted $M(H)$ measurements at various temperatures with a temperature interval of 10 K. These measurements were used to calculate magnetocaloric effect (MCE), whose magnitude is influenced by factors like magnetic field strength, material temperature, composition etc. Examining the MCE provides valuable insights into the material's properties, encompassing magnetic phase transitions, magnetic interactions, and entropy changes.

According to the classical Maxwell's thermodynamic relation[63–68], the isothermal magnetic entropy change can be expressed as follows:

$$\Delta S_M(T, H) = S_M(T, H) - S_M(T, 0) = \int_0^H \left(\frac{\partial M}{\partial T} \right)_H dH$$

Here, $\Delta S_M(T, H)$ represents the change in magnetic entropy, $S_M(T, H)$ and $S_M(T, 0)$ are the magnetic entropies at magnetic fields H and 0, respectively, and $\left(\frac{\partial M}{\partial T} \right)_H$ is the partial derivative of magnetization concerning temperature at a constant magnetic field H. This equation establishes a connection between the change in magnetic entropy and the derivative of magnetization with respect to temperature at a constant magnetic field. A substantial change in magnetic entropy near the magnetic transition temperature can be observed due to the equation's strong dependence on the value of $\left(\frac{\partial M}{\partial T} \right)$. The MCE is an exceptionally sensitive method for probing
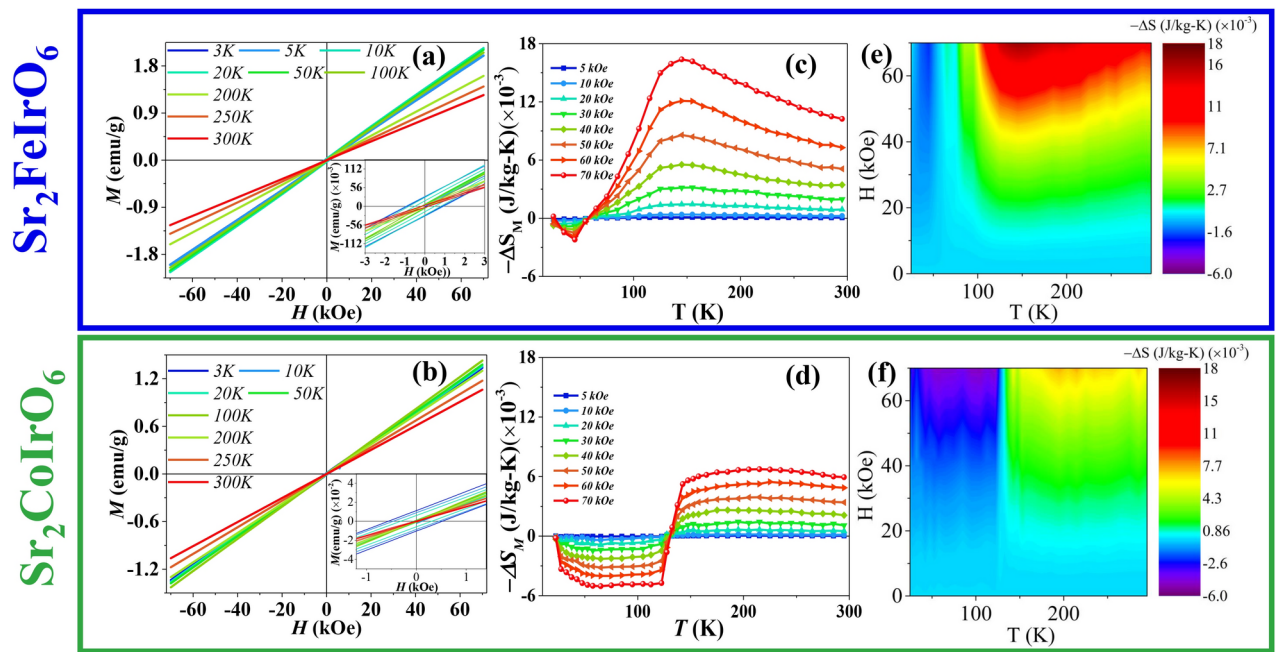
Fig. 6. Isotherm Magnetization at different temperature for (**a**) Sr_2FeIrO_6 and (**b**) Sr_2CoIrO_6 compound. Temperature dependence of the magnetic entropy change at various applied magnetic fields for (**c**), (**e**) Sr_2FeIrO_6 and (**d**),(**f**) Sr_2CoIrO_6 compounds.

magnetic phase transitions in compounds. In the case of simple FM like materials, the application of a magnetic field causes the magnetic moments to become more ordered along the direction of the magnetic field. As a result, the magnetic entropy of these materials decreases in the presence of the magnetic field, leading to an increase in $-\Delta S$ and producing a peak near the FM transition temperature. Conversely, in AFM systems, the application of an external magnetic field decreases the spin fluctuation of the magnetic sublattice parallel to the direction of the field. However, the enhanced spin fluctuation of the antiparallel sublattice results in an overall increase in magnetic entropy, which causes a sudden sign reversal of $-\Delta S$ from positive to negative below the Néel temperature. This sign reversal temperature corresponds to the AFM transition temperature[63–67].

In Fig. 6c for the SFI compound, an increase in $-\Delta S$ is observed with lowering temperature from 300K, peaking around 150 K, followed by a gradual decline. $-\Delta S$ changes sign from positive to negative around 60 K, near the T_N temperature. Figure 6e illustrates a 3D plot, depicting a hump-like gradient around 150 K and a slow, steady change. The positive ΔS signifies strong AFM correlations. However, the gradual variation also indicates the presence competing interaction in the compound. In Fig. 6d, the MCE for the SCI compound is depicted. Instead of showing a distinct peak, there is a sudden jump in $-\Delta S$ from a positive to a negative value around 130 K. Figure 6f further elucidates this abrupt change around 130 K with lowering temperature, indicating the presence of strong long-range AFM ordering.

To identify the presence of the glassy phase, we conducted magnetic relaxation ($M(t)$) and magnetic memory experiments. Both ZFC and FC protocols are commonly employed to investigate $M(t)$ behavior. For this study, we chose to utilize the ZFC protocol. The system was cooled from its paramagnetic state (T > 350 K) to the desired temperature without the application of an external magnetic field, allowing for a brief period to ensure temperature stabilization. Subsequently, the time-dependent magnetization was measured over an extended duration while applying a small magnetic field of 100 Oe.

Figure 7a and c depict the acquired relaxation curves for the SFI compound over a time period of time 5400 s at 10 K and 20 K, respectively. These curves demonstrate non-saturating and logarithmic behavior over time at the specified temperatures. Such slow magnetization evolution arises from thermal or quantum transitions amid numerous potential energy barriers, each associated with distinct relaxation times.

In glassy states, magnetic relaxation is described by stretched exponential functions, as expressed by the equation:

$$M(t) = M_0 + M_g \exp\left(-\left(\frac{t}{\tau}\right)^n\right)$$

Here, $M(t)$ signifies the magnetization at time t, M_0 represents the initial magnetization, M_g denotes a fitting parameter related to glassy component of magnetization, τ stands for the characteristic relaxation time, and n indicates the stretching exponent. This equation provides a mathematical representation of the observed time-dependent decay of magnetization in magnetic relaxation experiments.
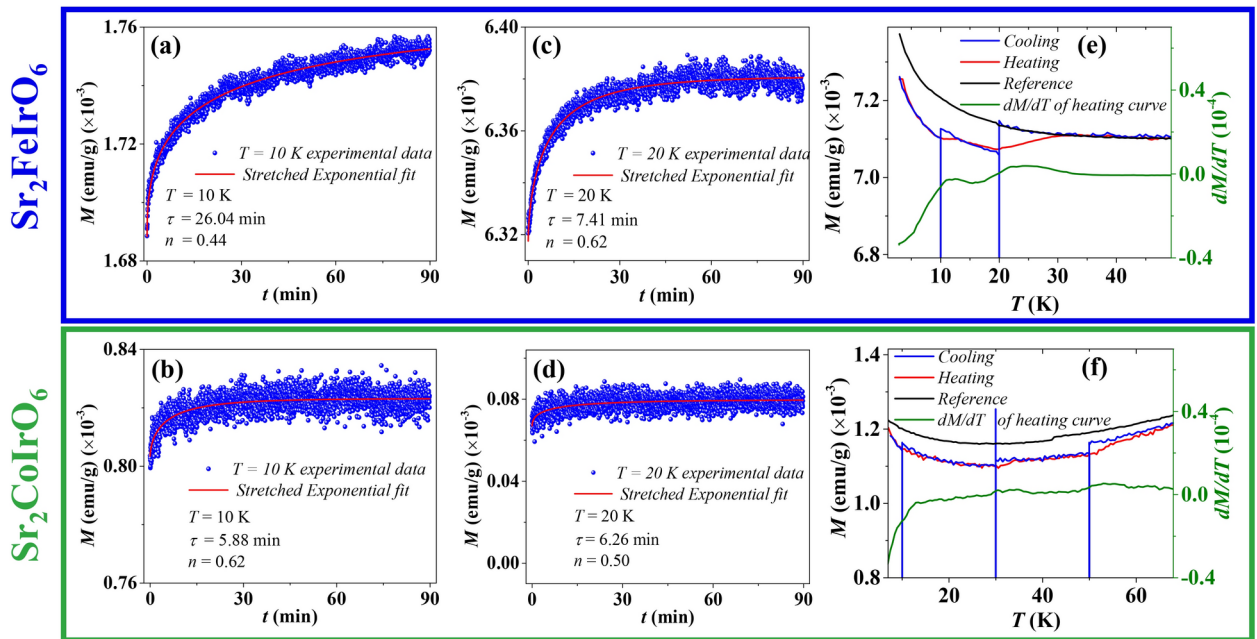
Fig. 7. The relaxation curves for Sr_2FeIrO_6, obtained from the ZFC protocol at (**a**) $T = 10$ K and (**c**) $T = 20$ K in the presence of $H = 100$ Oe; The relaxation curves for Sr_2CoIrO_6, obtained from the ZFC protocol at (**b**) $T = 10$ K and (**d**) $T = 20$ K in the presence of $H = 100$ Oe; Experimental data were fitted (red line) using Stretched Exponential function; Memory effect of (**e**) Sr_2FeIrO_6 and (**f**) Sr_2CoIrO_6 compound, where stops administered during cooling are recovered in heating, as seen in the derivative plots. A reference curve without stops is also presented for comparison.

To compare the relaxation behavior, it is essential to perform measurements for both compounds at the same temperature. However, since the transition temperature of SFI is nearly half that of SCI, we cannot conduct these experiments at higher temperatures. Additionally, we aim to perform the measurements at temperatures that allow sufficient intervals between consecutive data points. Therefore, we carried out the experiments at 10 K and 20 K, both well below the transition temperatures of both compounds. Furthermore, since 20 K is twice the value of 10 K, it provides a clear understanding of the temperature dependence.

For the SFI system at 10 K, τ is remarkably long, with a value of 26 minutes. The calculated *n* value is approximately 0.44, but with an increase in temperature to 20 K, τ is only 7 min., which is almost quadruple times less than the previous value. The observed magnetic relaxation behavior presents compelling evidence supporting the existence of a glassy phase in the SFI system at low temperature.

In contrast, SCI does not possess such a long relaxation time at 10 K and 20 K shown in Fig. 7b and d. The τ at 10 K is only 2.8 min with *n* value of 0.43. It does not change much at high temperatures. At 20 K, τ is 2.1 min, and β is 0.3. It clearly shows that SCI does not possess a glassy nature like SFI.

To understand the difference in relaxation behavior between these two compounds, we conducted magnetic memory experiments, a captivating phenomenon observed in frustrated spin systems. In the memory experiment, the sample is first cooled down to a low temperature at a constant rate while measuring the magnetization. During this cooling process, intermediate stops are introduced at regular intervals (45 min) below T_N, allowing the magnetization to relax. Once the temperature of 5 K is achieved, the sample is heated back up without any stops, and the magnetization is recorded. For comparison purposes, a reference curve is recorded with no intermediate stops. The cooling, heating, reference, and the derivative of the heating curve ($\frac{dM}{dT}$) are presented in Fig. 7e and f for the SFI and SCI compounds.

For SFI compound the cooling curve shows distinct "dips" in magnetization where the measurement was halted, while the heating cycle reveals signatures of the memory effect where the steps are retrieved at the same temperature points. These are clearly visible in the $\frac{dM}{dT}$ plot. On the contrary, the memory effect in the SCI compound is not distinctly visible, and in the $\frac{dM}{dT}$ plot, it appears nearly flat. The relaxation and memory effect experiments clearly indicate that SFI possesses a more pronounced glassy nature than SCI.

Based on the conducted experiments and analyses, it has been observed that there is a pronounced presence of strong AFM interaction in both compounds. However, what's particularly intriguing is that SFI exhibits disorder and spin glass behavior, whereas SCI does not manifest such behavior. In this context, it is interesting to investigate the presence and origin of EB in both systems. The shift of a material's hysteresis loop along both the field and magnetization axes can be conventionally described using two parameters. The first parameter is the EB field ($|H_{EB}| = |H_+ + H_-|/2$), quantifying the magnitude of the shift. The second parameter is the coercive field ($|H_C| = |H_+ - H_-|/2$), representing the strength of the magnetic field required to demagnetize

the material. The first and second intercepts of the magnetization curve with the field axis are denoted by H_+ and H_-, respectively.

ZFC and FC $M(H)$ measurements were conducted at 3 K using both ZFC and FC protocols. Figure 8a and b illustrate the $M(H)$ curves for the SFI and SCI compounds at 3 K with a magnetic field strength of 7 Tesla. The magnitudes of $|H_{EB}|$ and $|H_C|$ were determined from the $M(H)$ loops to be approximately 1.86 kOe and 1.77 kOe, respectively, for SFI. For SCI, the magnitudes of $|H_{EB}|$ and $|H_C|$ were determined to be 2.11 kOe and 1.13 kOe, respectively. The measurement of FC $M(H)$ has been conducted during the cooling process under both +7 Tesla and -7 Tesla magnetic fields. In each case, the value of the EB has yielded nearly identical values.

To investigate the temperature and cooling field (H_{CF}) dependence on EB, measurements were performed at 3 K with varying H_{CF} and at different temperatures with a constant H_{CF}. Figure 8c and d illustrate the H_{CF} dependency at 3 K. In both cases, EB increases with increasing H_{FC}.

Figure 8e and f depict the temperature dependence of H_{EB} for SFI and SCI compound, respectively. As temperature increases, H_{EB} exhibit a decrease and their behavior is effectively described by the following equations:

$$H_{EB}(T) = H_{EB}(0) \exp(-T/\beta) \tag{2}$$

Here, β represents a constant, and $H_{EB}(0)$ denotes the extrapolation of H_{EB} to absolute zero temperature. The values of H_{EB} and β for SFI are 2.06 kOe and 25.11 K, respectively. For SCI, the values of H_{EB} and β are 2.26 kOe and 36.89 K, respectively. The variation of the EB field with temperature suggests in case of SCI with increasing temperature EB decreases slowly compared to SFI.

Discussion

Here, we will delve into several factors. Initially, we'll investigate the influence of disorder, subsequently examining the consequences of lattice distortion. Finally, we will elucidate the origin of exchange bias.

In a perfectly ordered double perovskite (DP), the magnetism primary governed by Ir–O–Fe(Co)–O–Ir interaction. Each transition metal ion (Fe(Co)/Ir) in an ordered DP is surrounded by six other transition metal ions B′ (Ir/Fe(Co)) and exhibits AFM exchange interaction[55]. But due to the disorder this interaction chain breaks and give rise to another pair of interaction Fe–O–Fe(Co–O–Co) and Ir-O-Ir in SFI (SCI). Now discuss the new pair of interaction developed due to the disorder.

In the case of the SFI compound, if we consider the Fe–O–Fe interaction, Fe is in the Fe^{3+} state. The electronic configuration of Fe atoms can be described as a combination of $3d^5 L$ (Fe^{3+}), where the term L represents the ligand hole linked to the O 2p level. Since the Fe ions are in a high spin-state[69], they correspond to the configurations $t_{2g}^3 e_g^2$. In the case of the SCI compound, the electronic configuration for Co atoms is given by $3d^6 L$ (Co^{3+})[70]. The Co^{3+} ions are in the **high spin** state $t_{2g}^4 e_g^2$[71]. In both the SFI and SCI compounds, the in-
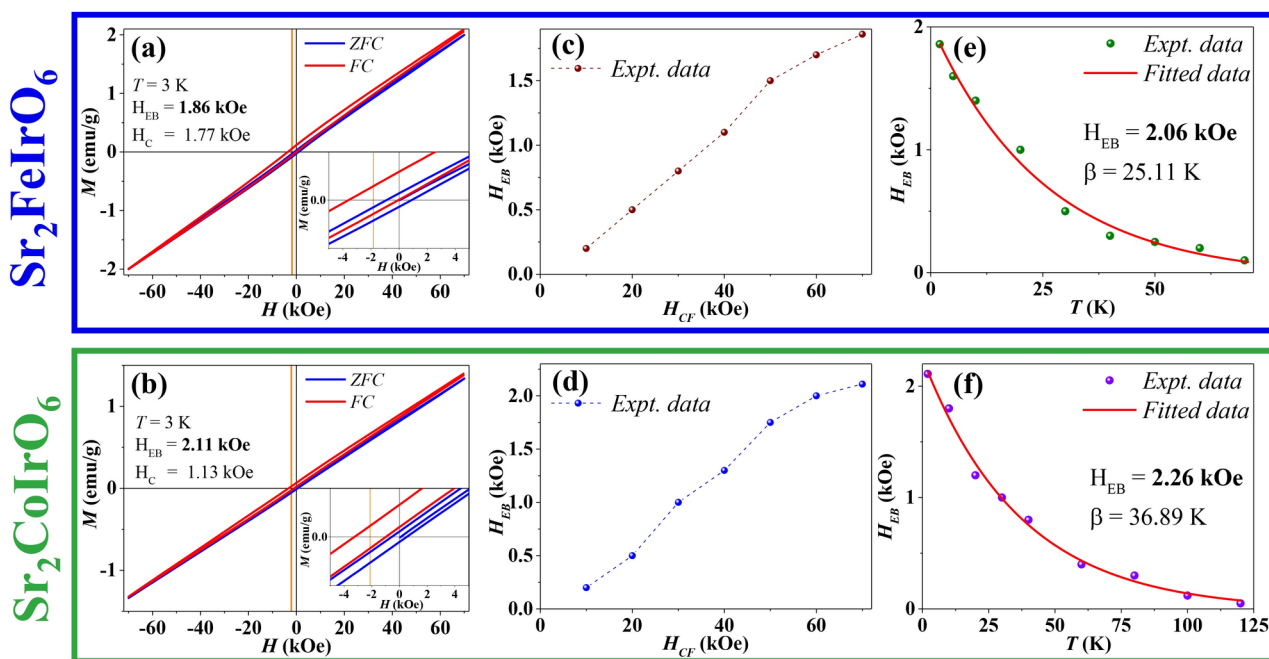

Fig. 8. $M(H)$ at $T = 3$ K in both ZFC and FC modes for (**a**) the Sr_2FeIrO_6 and (**b**) the Sr_2CoIrO_6 compound; and the dependence of EB on H_{FC} and temperature for (**c**) and (**e**) for the Sr_2FeIrO_6 compound, and (**d**) and (**f**) for the Sr_2CoIrO_6 compound.

plane Ir-Ir FM superexchange interaction is significantly smaller than the out-of-plane AFM interaction. For the in-plane FM interaction, electrons must hop from the Ir-t_{2g} subband to the Ir-e_g subband, which are separated by a substantial crystal field splitting of approximately 4 eV, making this process less probable. Conversely, electron hopping within the Ir-t_{2g} manifold is more likely, resulting in AFM interactions along the out-of-plane direction[55].

Among the newly introduced interactions the interaction between Fe-Fe and Co-Co pairs is highly dependent on the crystallographic direction. For Fe-Fe pairs, the out-of-plane interaction is AFM, while the in-plane interaction is FM[55,72]. However, the strength of the AFM interaction is much greater than that of the FM interaction. A similar behavior is observed for Co-Co interactions[73]. Thus, the overall interaction can be considered predominantly antiferromagnetic in nature[74]. Structural analysis indicates that the out-of-plane bond angles are significantly more distorted in the SFI compound compared to the SCI compound. This distortion weakens the AFM interactions in SFI relative to SCI. These magnetic alteration due to the ionic disorder and structural distortion are reflected in the MCE measurements, where a broad hump is observed in SFI but a sharp transition is observed in the SCI compound. Now, SFI experiences frustration due to these competing exchange interactions.

This observation supports the experimental findings, indicating a transition temperature of 60 K with a negative and larger value of θ_P ($-$ 168K) compared to SCI's transition temperature of 130 K with a θ_P value of $-$ 155K.

This observation supports the experimental finding that SFI (60 K) exhibits a lower transition temperature than SCI (130 K). In the relaxation and memory experiments, we also observed that SFI exhibits glassy behavior, whereas SCI does not display such frustration.

Our experimental findings indicate the presence of EB in both compounds. The SFI compound, which exhibits a higher degree of ionic disorder and more pronounced spin-glass behavior, contains FM/AFM, FM/SG, and SG/AFM interfaces, resulting in an exchange bias of 1.86 kOe, consistent with conventional theory[75,76]. However, it is not commonly reported that a purely antiferromagnetic material can exhibit exchange bias, and the understanding of this phenomenon remains an active area of research. Recently, Asakura et al.[19] have demonstrated for the first time that a purely antiferromagnetic system can exhibit EB, albeit the underlying mechanism is not fully understood. Surprisingly, in our SCI compound, despite the absence of magnetic memory and relaxation behavior, we observed an even higher exchange bias of 2.11 kOe. If the EB were solely attributed to disorder and spin-glass characteristics, we would expect a significantly lower value. This unexpected result suggests that, beyond spin-glass effects, an underlying antiferromagnetic mechanism also contributes to the EB in SCI. Additionally, our MCE analysis revealed strong AFM interactions in SCI. Collectively, these findings suggest that the EB in SCI predominantly originates from its AFM structure, distinguishing it as unique. Consequently, conventional theoretical frameworks are inadequate for fully explaining the EB observed in these compounds. Now, Ir is known for its strong spin-orbit coupling properties. The electronic structure calculations indicate that spin-orbit coupling enhances the noncollinear antiferromagnetic ordering, stabilizing a ground state defined by a Mott-type insulating phase in these Ir-based double perovskites[40,55]. This noncollinear antiferromagnetic structure plays a crucial role in the existence of EB in these AFM material[19]. When considering the interactions between Ir/Co and Ir/Fe, the presence of Dzyaloshinskii-Moriya (DM) interaction becomes highly plausible[62,77–80]. Dong et al. have proposed that certain noncollinear antiferromagnetic systems can exhibit EB through DM interaction. In Ir-based double perovskite systems, the DM interaction, coupled with the noncollinear magnetic structure, promotes the emergence of EB phenomena within the compound[30–32].

Conclusion

In summary, we utilized the solid-state reaction method to synthesize polycrystalline SFI and SCI compounds. The quality of the samples was evaluated through XRD measurements and Rietveld analysis, revealing that both compounds maintain triclinic structural symmetry. The polycrystalline nature and quality of the sample were analyzed through SEM and TEM analysis. Through HRTEM analysis, we observed the ordered arrangement of Co and Ir in SCI.

Through this structural and magnetic study of the 3d–5d element-based double perovskite, it becomes apparent that despite Fe and Co being neighboring elements in the 3d series of the periodic table, they display distinct magnetic properties influenced by their ionic disorder and lattice distortion. While both crystalline structures are triclinic, SFI exhibits more ionic disorder and structural distortion than SCI, leading to the development of FM correlation, resulting in frustration and glassy behavior in SFI.

Both compounds exhibit EB, but the origin differs significantly between them. In the case of the SFI compound, EB arises from the interactions between FM/SG, AFM/FM, and SG/AFM, resulting from the ionic disorder. However, for SCI, the origin of EB is less obvious. In MCE calculations, a sharp transition due to AFM ordering is observed in SCI. The EB characteristics can be analyzed through theoretical frameworks proposed by Dong et al., wherein the DM interaction plays a pivotal role in eliciting EB within spin-compensated AFM systems. In summary, our findings on these compounds will pave the way for future research on exchange bias in spin-compensated materials, which is crucial for potential applications in ultra-fast antiferromagnetic spintronic devices.

Data availability

The data that support the findings of this study are available from the corresponding author upon reasonable request.

References

1. Baltz, V. et al. Antiferromagnetic spintronics. *Rev. Mod. Phys.* **90**, 015005 (2018).
2. Jungwirth, T., Marti, X., Wadley, P. & Wunderlich, J. Antiferromagnetic spintronics. *Nat. Nanotechnol.* **11**, 231 (2016).
3. Gomonay, O., Jungwirth, T. & Sinova, J. Concepts of antiferromagnetic spintronics. *Phys. Status Solidi (RRL) Rapid Res. Lett.* **11**, 1700022 (2017).
4. Han, J., Cheng, R., Liu, L., Ohno, H. & Fukami, S. Coherent antiferromagnetic spintronics. *Nat. Mater.* **22**, 684 (2023).
5. Oh, Y.-W. et al. Field-free switching of perpendicular magnetization through spin-orbit torque in antiferromagnet/ferromagnet/oxide structures. *Nat. Nanotechnol.* **11**, 878 (2016).
6. Oh, Y.-W. et al. Field-free switching of perpendicular magnetization through spin-orbit torque in antiferromagnet/ferromagnet/oxide structures. *Nat. Nanotechnol.* **11**, 878 (2016).
7. Fukami, S., Zhang, C., DuttaGupta, S., Kurenkov, A. & Ohno, H. Magnetization switching by spin-orbit torque in an antiferromagnet-ferromagnet bilayer system. *Nat. Mater.* **15**, 535 (2016).
8. Peng, S. et al. Exchange bias switching in an antiferromagnet/ferromagnet bilayer driven by spin-orbit torque. *Nat. Electron.* **3**, 757 (2020).
9. Pandey, P. et al. Electronic control of interface ferromagnetic order and exchange-bias in paramagnetic-antiferromagnetic epitaxial bilayers. *Nanoscale* **7**, 3292 (2015).
10. Rana, R., Pandey, P. & Rana, D. S. Controlling the coexisting vertical magnetization shift and exchange bias in La0. 3Sr0. 7FeO3/SrRuO3 bilayers. *Applied Physics Letters* **104** (2014).
11. Ong, Q. K., Wei, A. & Lin, X.-M. New magnetic anisotropy. *Phys. Rev. B* **80**, 134418 (2009).
12. Pandey, P., Rana, R., Tripathi, S. & Rana, D. S. Effect of structural and magnetic exchange coupling on the electronic transport of NdNiO3 films intercalated with La0. 7Sr0. 3MnO3 thin layers. *Applied Physics Letters* **103** (2013).
13. Mishra, S., Radu, F., Dürr, H. & Eberhardt, W. Training-induced positive exchange bias in NiFe/IrMn bilayers. *Phys. Rev. Lett.* **102**, 177208 (2009).
14. Gibert, M., Zubko, P., Scherwitzl, R., Íñiguez, J. & Triscone, J.-M. Exchange bias in LaNiO$_3$-LaMnO$_3$ superlattices. *Nat. Mater.* **11**, 195 (2012).
15. Pal, K. & Das, I. The Impact of Oxygen Deficiency on Giant Exchange Bias in Perovskite Oxide: SrFe$_{0.5}$Co$_{0.5}$O$_3$-δ ($\delta = 0.37$). *Journal of Alloys and Compounds* **170794** (2023).
16. Testa-Anta, M., Rivas-Murias, B. & Salgueiriño, V. Spin frustration drives exchange bias sign crossover in CoFe$_2$O$_4$-Cr$_2$O$_3$ nanocomposites. *Adv. Func. Mater.* **29**, 1900030 (2019).
17. Rana, R., Pandey, P., Singh, R. P. & Rana, D. S. Positive exchange-bias and giant vertical hysteretic shift in La0. 3Sr0. 7FeO3/SrRuO3 bilayers. *Sci. Rep.* **4**, 4138 (2014).
18. Pal, K. & Das, I. Exploring the exchange bias of Gd and MnPt: A combined structural and magnetic investigation. *Thin Solid Films* **790**, 140211 (2024).
19. Asakura, M. et al. Observation of omnidirectional exchange bias at all antiferromagnetic polycrystalline heterointerface. *Advanced Materials* **2400301** (2024).
20. Ou, X., Li, Z., Fan, F., Wang, H. & Wu, H. Long-range magnetic interaction and frustration in double perovskites Sr$_2$NiIrO$_6$ and Sr$_2$ZnIrO$_6$. *Sci. Rep.* **4**, 7542 (2014).
21. Vasala, S., Yamauchi, H. & Karppinen, M. Synthesis, crystal structure and magnetic properties of a new B-site ordered double perovskite Sr$_2$CuIrO$_6$. *J. Solid State Chem.* **220**, 28 (2014).
22. Kharkwal, K., Patel, R. K., Asokan, K. & Pramanik, A. Structural, magnetic and dielectric properties in 3d–5d based Sr$_2$FeIrO$_6$ thin films. *J. Phys.: Condens. Matter* **32**, 505001 (2020).
23. Agrestini, S. et al. Nature of the magnetism of iridium in the double perovskite Sr$_2$ CoIrO $_6$. *Phys. Rev. B* **100**, 014443 (2019).
24. Pesin, D. & Balents, L. Mott physics and band topology in materials with strong spin-orbit interaction. *Nat. Phys.* **6**, 376 (2010).
25. Jackeli, G. & Khaliullin, G. Mott insulators in the strong spin-orbit coupling limit: from Heisenberg to a quantum compass and Kitaev models. *Phys. Rev. Lett.* **102**, 017205 (2009).
26. Wang, F. & Senthil, T. Twisted Hubbard model for Sr$_2$IrO$_4$: magnetism and possible high temperature superconductivity. *Phys. Rev. Lett.* **106**, 136402 (2011).
27. Wan, X., Turner, A. M., Vishwanath, A. & Savrasov, S. Y. Topological semimetal and Fermi-arc surface states in the electronic structure of pyrochlore iridates. *Phys. Rev. B* **83**, 205101 (2011).
28. Balents, L. Spin liquids in frustrated magnets. *Nature* **464**, 199 (2010).
29. Chaloupka, J., Jackeli, G. & Khaliullin, G. Kitaev-Heisenberg model on a honeycomb lattice: Possible exotic phases in iridium oxides A$_2$IrO$_3$. *Phys. Rev. Lett.* **105**, 027204 (2010).
30. Dong, S. et al. Exchange bias driven by the Dzyaloshinskii-Moriya interaction and ferroelectric polarization at G-type antiferromagnetic perovskite interfaces. *Phys. Rev. Lett.* **103**, 127201 (2009).
31. Yanes, R., Jackson, J., Udvardi, L., Szunyogh, L. & Nowak, U. Exchange bias driven by Dzyaloshinskii-Moriya interactions. *Phys. Rev. Lett.* **111**, 217202 (2013).
32. Dzyaloshinsky, I. A thermodynamic theory of "weak" ferromagnetism of antiferromagnetics. *J. Phys. Chem. Solids* **4**, 241 (1958).
33. Roisnel, T., & Rodriguez-Carvajal, J. WinPLOTR: A Windows Tool for Powder Diffraction Patterns Analysis, in *Proceedings of the Seventh European Powder Diffraction Conference (EPDIC 7)*, edited by R. Delhez and E. Mittenmeijer (Materials Science Forum, 2000) pp. 118–123.
34. Rodriguez-Carvajal, J. Recent developments of the program FULLPROF. *Phys. B* **192**, 55 (1993).
35. Momma, K. & Izumi, F. VESTA: a three-dimensional visualization system for electronic and structural analysis. *J. Appl. Crystallogr.* **41**, 653 (2008).
36. Qasim, I. et al. Ordered vs. disordered perovskites; structural studies of Fe-doped SrIrO3 and SrRuO3. *J. Solid State Chem.* **206**, 242 (2013).
37. Narayanan, N. et al. Temperature and composition dependence of crystal structures and magnetic and electronic properties of the double perovskites La 2–x Sr x CoIrO 6 (0= x= 2). *Phys. Rev. B-Condens. Matt. Mater. Phys.* **82**, 024403 (2010).
38. Bufaiçal, L. et al. Physical properties of Sr2FeIrO6 and Sr1. 2La0. 8FeIrO6 double perovskites obtained by a new synthesis route. *Mater. Chem. Phys.* **182**, 459 (2016).
39. Guo, Y. et al. Synthesis of La1-xSrxCoO3-δ and its catalytic oxidation of NO and its reaction path. *Heliyon* **10** (2024).
40. Kharkwal, K. et al. Structure, magnetism, and electronic properties in 3 d-5 d based double perovskite (Sr 1–x Ca x) 2 FeIrO 6 (0= x= 1). *Phys. Rev. B* **102**, 174401 (2020).
41. Huelser, T., Schnurre, S., Wiggers, H., & Schulz, C. Gasphase synthesis of highly-specific nanoparticles on the pilot-plant scale, in *Proceedings of world congress on particle technology (WCPT6)* (2010).
42. Zhong, Y. et al. Microwave-assisted synthesis of Fe$_3$ O$_4$ nanocrystals with predominantly exposed facets and their heterogeneous UVA/Fenton catalytic activity. *ACS Appl. Mater. Interf.* **9**, 29203 (2017).
43. Su, J., Lu, X., Zhang, J., Sun, H., Zhang, C., Jiang, Z., Ju, C., Wang, Z., Huang, F., & Zhu, J. The effect of Fe^{2+} ions on dielectric and magnetic properties of Yb$_3$Fe$_5$O$_{12}$ ceramics, Journal of Applied Physics **111** (2012).

44. Rajan, A., Sharma, M. & Sahu, N. K. Assessing magnetic and inductive thermal properties of various surfactants functionalised Fe_3O_4 nanoparticles for hyperthermia. *Sci. Rep.* **10**, 15045 (2020).

45. Dwivedi, V. K. & Mukhopadhyay, S. Suppression of long range magnetic ordering and electrical conduction in $Y_{1.7}Bi_{0.3}Ir_2O_7$ thin film. *J. Magn. Magn. Mater.* **484**, 313 (2019).

46. Dwivedi, V. K. & Mukhopadhyay, S. Coexistence of high electrical conductivity and weak ferromagnetism in Cr doped $Y_2Ir_2O_7$ pyrochlore iridates. *Journal of Applied Physics* **125** (2019).

47. Duan, Q., & Chen, H. Synthesis and electrochemical properties of Co_3O_4 nanoparticles by hydrothermal method at different temperatures,in *IOP Conference Series: Materials Science and Engineering*, Vol. 207 (IOP Publishing, 2017) p. 012020.

48. Alex, C., Sarma, S. C., Peter, S. C. & John, N. S. Competing effect of Co^{3+} reducibility and oxygen-deficient defects toward high oxygen evolution activity in Co_3O_4 systems in alkaline medium. *ACS Appl. Energy Mater.* **3**, 5439 (2020).

49. Das, R. R. et al. Giant exchange bias effect in Ruddlesden-Popper oxides SrLaFe0. 25+ xMn0. 25Co0. 5- xO4 (x= 0, 0.25): Role of the cluster glass magnetic phase in a quasi-two-dimensional perovskite. *Phys. Rev. B* **102**, 134405 (2020).

50. Naveen, K. et al. Reentrant magnetism at the borderline between long-range antiferromagnetic order and spin-glass behavior in the B-site disordered perovskite system C a 2–x S rx FeRu O 6. *Phys. Rev. B* **98**, 224423 (2018).

51. Su, C. et al. Type-II antiferromagnetic ordering in the double perovskite oxide Sr_2NiWO_6. *Phys. Rev. B* **108**, 054416 (2023).

52. Manna, K. et al. Noncollinear antiferromagnetism of coupled spins and pseudospins in the double perovskite La_2CuIrO_6. *Phys. Rev. B* **94**, 144437 (2016).

53. Zhu, W. et al. Strong ferromagnetism induced by canted antiferromagnetic order in double perovskite iridates $(La_{1-x}$ Sr $_x)_2$ $ZnIrO_6$. *Phys. Rev. B* **91**, 144408 (2015).

54. Ferreira, T., Morrison, G., Yeon, J. & zur Loye, H.-C. Design and Crystal Growth of Magnetic Double Perovskite Iridates: Ln_2 $MIrO_6$ (Ln= La, Pr, Nd, Sm-Gd; M= Mg, Ni). *Crystal Growth & Design* **16**, 2795 (2016).

55. Roy, R. & Kanungo, S. First principles investigation of spin-orbit coupling driven magnetism of the 3d–5d double-perovskite (Sr/ Ca)$_2$$FeIrO_6$. *Phys. Rev. B* **106**, 125113 (2022).

56. Cao, G. et al. Novel magnetism of Ir 5+(5 d 4) ions in the double perovskite Sr_2YIrO_6. *Phys. Rev. Lett.* **112**, 056402 (2014).

57. Pajskr, K. et al. On the possibility of excitonic magnetism in Ir double perovskites. *Phys. Rev. B* **93**, 035129 (2016).

58. Laguna-Marco, M. et al. Magnetism of Ir 5+-based double perovskites: Unraveling its nature and the influence of structure. *Phys. Rev. B* **101**, 014449 (2020).

59. Lee, M.-C. et al. Hybridized orbital states in spin-orbit coupled 3 d- 5 d double perovskites studied by x-ray absorption spectroscopy. *Phys. Rev. B* **97**, 125123 (2018).

60. Mardegan, J. et al. 3 d and 5 d electronic structures and orbital hybridization in Ba-and Ca-doped La 2 CoIrO 6 double perovskites. *Phys. Rev. B* **107**, 214427 (2023).

61. Narayanan, N. et al. Temperature and composition dependence of crystal structures and magnetic and electronic properties of the double perovskites. *Phys. Rev. B* **82**, 024403 (2010).

62. Zhou, J.-S., Marshall, L., Li, Z.-Y., Li, X. & He, J.-M. Weak ferromagnetism in perovskite oxides. *Phys. Rev. B* **102**, 104420 (2020).

63. Tishin, A., Gschneidner, K. Jr. & Pecharsky, V. Magnetocaloric effect and heat capacity in the phase-transition region. *Phys. Rev. B* **59**, 503 (1999).

64. Das, I. & Rawat, R. A study of magnetocaloric effect in PrCo2Si2 to understand contributions to magnetoresistance. *Solid State Commun.* **115**, 207 (2000).

65. Samanta, T., Das, I. & Banerjee, S. Giant magnetocaloric effect in antiferromagnetic ErRu2Si2 compound. *Applied Physics Letters* **91** (2007).

66. Samanta, T., Das, I. & Banerjee, S. Comparative studies of magnetocaloric effect and magnetotransport behavior in GdRu2Si2 compound. *Journal of Applied Physics* **104** (2008).

67. Von Ranke, P. et al. Understanding the inverse magnetocaloric effect in antiferro-and ferrimagnetic arrangements. *J. Phys.: Condens. Matter* **21**, 056004 (2009).

68. Pal, K. & Das, I. Exploring the origin of exchange bias and spin glass behavior in 6H hexagonal perovskite structure: Structural and magnetic analysis. *Appl. Mater. Today* **39**, 102316 (2024).

69. Abbate, M. et al. Controlled-valence properties of $La_{1-x}Sr_xFeO_3$ and $La_{1-x}Sr_xMnO_3$ studied by soft-x-ray absorption spectroscopy. *Phys. Rev. B* **46**, 4511 (1992).

70. Abbate, M. et al. Controlled-valence properties of $La_{1-x}Sr_xFeO_3$ and $La_{1-x}Sr_xMnO_3$ studied by soft-x-ray absorption spectroscopy. *Phys. Rev. B* **65**, 165120 (2002).

71. Potze, R., Sawatzky, G. & Abbate, M. Possibility for an intermediate-spin ground state in the charge-transfer material SrCoO 3. *Phys. Rev. B* **51**, 11501 (1995).

72. Kanungo, S., Yan, B., Jansen, M. & Felser, C. Ab initio study of low-temperature magnetic properties of double perovskite Sr 2 FeOsO 6. *Phys. Rev. B* **89**, 214414 (2014).

73. Yan, B. et al. Lattice-site-specific spin dynamics in double perovskite Sr 2 CoOsO 6. *Phys. Rev. Lett.* **112**, 147202 (2014).

74. Serrate, D., De Teresa, J. & Ibarra, M. Double perovskites with ferromagnetism above room temperature. *J. Phys.: Condens. Matter* **19**, 023201 (2006).

75. Bufaiçal, L. & Bittar, E. Essential aspects of the spontaneous exchange bias effect. *Journal of Magnetism and Magnetic Materials* **172109** (2024).

76. Liu, P. et al. Respective dependencies of conventional and spontaneous exchange biases on spin glass. *Phys. Rev. B* **109**, 184412 (2024).

77. Nickel, F., Meyer, S. & Heinze, S. Exchange and Dzyaloshinskii-Moriya interaction in Rh/Co/Fe/Ir multilayers: Towards skyrmions in exchange-frustrated multilayers. *Phys. Rev. B* **107**, 174430 (2023).

78. Meyer, S., Dupé, B., Ferriani, P. & Heinze, S. Dzyaloshinskii-Moriya interaction at an antiferromagnetic interface: First-principles study of Fe/Ir bilayers on Rh (001). *Phys. Rev. B* **96**, 094408 (2017).

79. Kim, N.-H. et al. Interfacial Dzyaloshinskii-Moriya interaction, surface anisotropy energy, and spin pumping at spin orbit coupled Ir/Co interface. *Applied physics letters* **108** (2016).

80. Kloodt-Twesten, F., Kuhrau, S., Oepen, H. P. & Frömter, R. Measuring the Dzyaloshinskii-Moriya interaction of the epitaxial Co/ Ir (111) interface. *Phys. Rev. B* **100**, 100402 (2019).

Acknowledgements

Conflict of interest

The authors declare no potential conflict of interest.

Additional information

Supplementary Information The online version contains supplementary material available at https://doi.org/10.1038/s41598-024-76130-5.

Correspondence and requests for materials should be addressed to K.P.

Reprints and permissions information is available at www.nature.com/reprints.

Publisher's note Springer Nature remains neutral with regard to jurisdictional claims in published maps and institutional affiliations.